Spectroscopic signatures of plasmonic near-fields on high-harmonic emission

Jalil, Sohail A.; Awan, Kashif M.; Baxter, Joshua; Bart, Graeme; Purschke, David N.; Fennel, Thomas; Villeneuve, David M.; Staudte, André; Berini, Pierre; Brabec, Thomas; Ramunno, Lora; Vampa, Giulio

Publisher's version / Version de l'éditeur:
https://doi.org/10.1002/lpor.202300448
Laser & Photonics Reviews, 17, 2023-10-20

LASER & PHOTONICS REVIEWS
www.lpr-journal.org

Spectroscopic Signatures of Plasmonic Near-Fields on High-Harmonic Emission

*Sohail A. Jalil, Kashif M. Awan, Joshua Baxter, Graeme Bart, David N. Purschke, Thomas Fennel, David M. Villeneuve, André Staudte, Pierre Berini, Thomas Brabec, Lora Ramunno, and Giulio Vampa**

Intense laser fields can reveal the attosecond and femtosecond response of matter in the emitted photoelectrons and high-harmonic photons. The complementary perspective offered by these two messengers is well explored in gas molecules and, more recently, in bulk solids, where both electron emission and high-order harmonics have been utilized to probe the laser-matter interaction. In nanoscale solids, electron emission provides a wealth of information about the localized and inhomogeneous near fields around the nanoparticles. Here, it is shown experimentally that inhomogeneous fields also affect high-order harmonics. Specifically, the experiment reveals strong indications that the field gradient of a nanoscale plasmonic hotspot found inside a Si crystal induces the emission of even-order high harmonics from the crystal itself. This demonstration extends the complementary electron-photon perspective on attosecond science to nanoscale systems.

1. Introduction

The attosecond and femtosecond response of homogeneous matter to intense laser fields can be revealed with both photoelectrons[1–4, 7] and high-harmonic photons.[5, 6, 8–12] On the other hand, a laser field that irradiates a nanoscale[1–16] system, e.g., metallic nanotips,[13,14,17] silica nanospheres,[15,16] and clusters,[18] creates a localized hotspot of intense near-field radiation that triggers ionization and the release of photoelectrons. The photoelectron kinetic energy and emission angle have revealed detailed information about the distribution of the electric field surrounding nanoscale objects, and its effect on high-field interactions. For instance, photoelectrons can be accelerated outside the hotspot within a small fraction of the laser cycle, thereby clamping their maximum kinetic energy,[14] or can reveal the attosecond-fast modulation of ionization[19] and the onset of space charge.[17] In silica nanospheres, the strong near-fields at their surface control the final photoelectron momentum.[15]

Recently, probing strong-field interactions in nanoscale systems with light has become possible with the observation of high-harmonic emission from plasmonic[20–22] and dielectric nanostructures and metasurfaces.[23–27] With one exception,[25]

S. A. Jalil, D. N. Purschke, D. M. Villeneuve, A. Staudte, G. Vampa
Joint Attosecond Science Laboratory
National Research Council of Canada and University of Ottawa
Ottawa, Ontario K1N 0R6, Canada
E-mail: gvampa@uottawa.ca

K. M. Awan
Institute of Materials Science and Engineering
Washington University in St. Louis
St. Louis, MO 63130, USA

The ORCID identification number(s) for the author(s) of this article can be found under https://doi.org/10.1002/lpor.202300448

DOI: 10.1002/lpor.202300448

K. M. Awan
Department of Mechanical Engineering and Materials Science
Washington University in St. Louis
St. Louis, MO 63130, USA

J. Baxter, P. Berini, L. Ramunno
Centre for Research in Photonics
University of Ottawa
25 Templeton Street, Ottawa, Ontario K1N 6N5, Canada

J. Baxter, G. Bart, P. Berini, T. Brabec, L. Ramunno
Department of Physics
University of Ottawa
150 Louis Pasteur, Ottawa, Ontario K1N 6N5, Canada

T. Fennel
Institute for Physics
University of Rostock
18051 Rostock, Germany

P. Berini
School of Electrical Engineering and Computer Science
University of Ottawa
800 King Edward Avenue, Ottawa, Ontario K1N 6N5, Canada

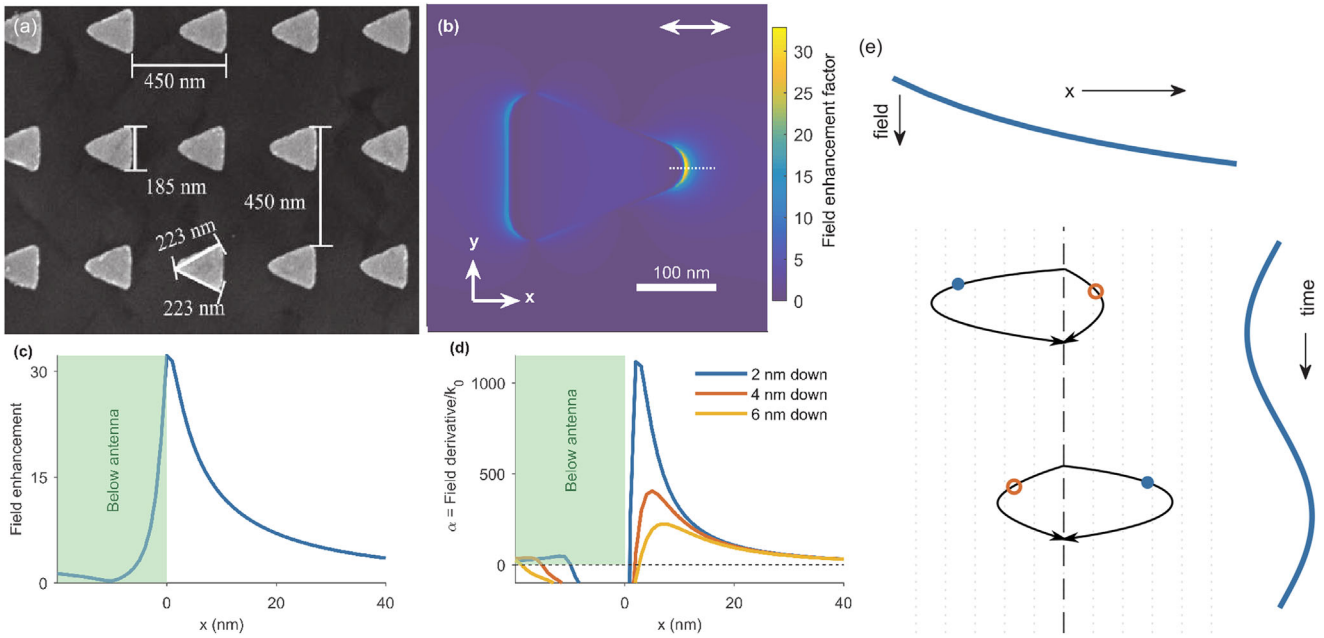

Figure 1. Role of the inhomogeneous field in the hotspot. a) Scanning electron micrograph of the fabricated Au triangular nanoantennas on a Si substrate. The antenna dimensions are chosen such that the metasurface resonates at the driving wavelength of 2.04 μm. b) Simulated field enhancement of the electric field component E_x parallel to the antenna's major axis (marked by the double-sided arrow), 2 nm below the Si surface. The incoming infrared field is also polarized parallel to the antennas' axis. The field is mostly enhanced near the antenna's apex. c) A lineout of the field along the dotted line of panel (b). The field decays rapidly over few nanometers. d) Field gradient parameter α as a function of "x". The gradient remains very large (hundreds of free-space wavevectors, k_0) even a few nanometers below the surface. Given the short absorption length of above-gap radiation, high harmonics are generated exclusively near the surface, likely within these high gradients. e) Sketch of electron (blue circles) and hole (hollow red circles) trajectories during two subsequent laser half cycles in the inhomogeneous field of the hotspot (top blue curve). Because electrons (and holes) travel to regions of different field strength in the two half cycles, their trajectory is not mirror symmetric. This asymmetry results in the appearance of even-order harmonics.

all prior experiments demonstrated enhanced high-harmonic generation in the driving field hotspot defined by the nanostructures. However, high-harmonic experiments have not yet conveyed the insightful information about the near-field interaction that photoelectron experiments have.

This lack of evidence is surprising, considering that electrons responsible for high-harmonic emission are accelerated on closed paths that bring them to collide with their correlated ion (in gases[28]) or hole (in solids[10]). In solids, these paths can be quite extended, from a few to several nanometers,[29] thus comparable to the volume over which photoelectrons are accelerated near nanostructures.[14] It is plausible, then, that the traveling electrons can sense the inhomogeneity of the driving laser field and encode it on the high-harmonic spectrum. Here, we show experimentally that the inhomogeneity of the hotspot perturbs high-harmonic generation at the microscopic level and leads to the appearance of even-order high harmonics.

2. Results and Discussion

To demonstrate the effect of the plasmonic field gradient on high-harmonic generation (also interpreted as a non-dipolar effect[30]), we design and fabricate triangular gold nanoantennas on a single-crystal silicon film (**Figure 1**a) and irradiate them at their resonance (free-space) wavelength of 2 μm, with 80 fs pulses with a peak intensity of 0.23 TW cm^{-2} (see Data S1, Supporting Information for the antennas' spectrum).

The excitation of the localized plasmon resonance causes extreme localization of the incident laser field to a nanoscale hotspot (Figure 1b), where the field becomes strongly inhomogeneous (Figure 1c). The localized field can be parametrized as a multipolar expansion:

$$F(x) \propto e^{-kx} \simeq 1 - kx + O\left(x^2\right) \quad (1)$$

where the first term represents a uniform field (dipole approximation), and the second term is the lowest-order non-dipolar contribution. In the hotspot, the gradient of the field is $k = \alpha k_0 \gg k_0 = \frac{2\pi}{\lambda} = 3.14\ \mu m^{-1}$ (k_0 is the free-space vacuum wavevector, α is the field gradient parameter). Figure 1d shows that α can reach values exceeding 1000, 2 nm below the surface. Assuming the electron travels one lattice site ($x \approx 0.5$ nm), even a modest value of $\alpha = 200$ results in non-dipolar relative field modification across the excursion length on the order of ≈ 0.3, comparable to the dipolar term.

Owing to the increased field strength in the hotspot, high-harmonic generation preferentially takes place in this small, highly inhomogeneous volume. As sketched in Figure 1e, electrons (holes) created within this volume in the first laser half-cycle are accelerated toward increasing (decreasing) field strength. At the subsequent laser half-cycle, the field direction flips so that the electron (hole) travels toward lower

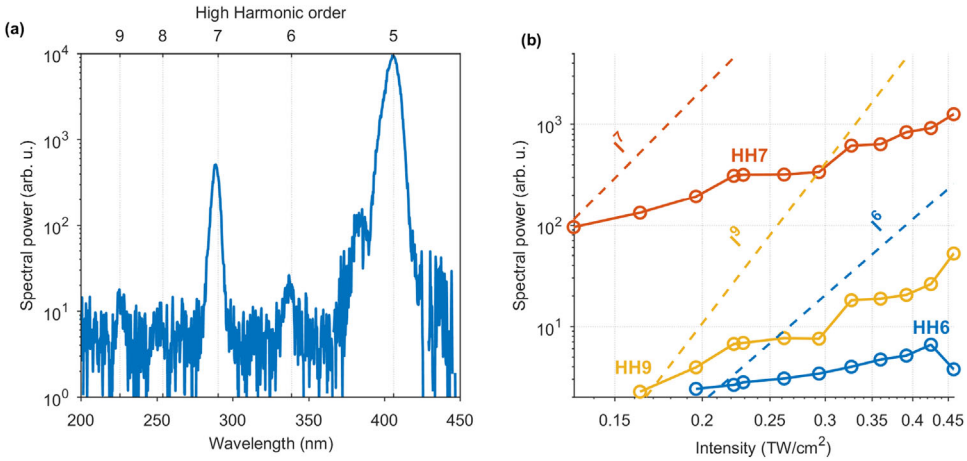

Figure 2. Spectral signatures of field gradient. a) Weak even harmonic orders (6th and 8th) are observed alongside the odd harmonics when irradiating triangular nanoantennas. b) All high harmonics scale non-perturbatively with the incident laser intensity. Dashed lines are power-law scaling expected for perturbative harmonics. The reported intensity is that incident on the sample (not accounting for enhancement).

(higher) fields. Because of the broken symmetry between trajectories in successive laser half-cycles, even-order harmonics are generated, as shown in the measured spectrum of **Figure 2**a.

Generation of high-order even harmonics from nanoantennas has been predicted,[31,32] but never observed experimentally, although second harmonic generation has been measured in the perturbative regime.[33] Instead, our high harmonics scale non-perturbatively with the driving laser intensity (Figure 2b) and thus a more appropriate physical interpretation relies on strongly driven electron-hole pairs, as we discuss in the next section. The triangular shape of the antennas is crucial to reveal this asymmetry: left-right symmetric antennas average out this effect because in each half cycle electrons travel simultaneously toward the high and low fields on either side of the antenna. Indeed, Data S2 (Supporting Information) and Ref.[20] show that only odd-order harmonics are emitted from rectangular antennas. Even the triangular antenna utilized in this work, despite the significantly lower field enhancement on the left side, is not quite enough to reveal the full asymmetry (see Materials and Methods in Supporting Information). To further reveal the role of field enhancement, in Data S7 (Supporting Information) we show that emission from triangular antennas exists over a broader range of pump polarization orientations than in rectangular antennas, in agreement with a wider opening angle of the antennas' apex.

To model the asymmetry, we calculate the semiclassical trajectories in Si, in the spatially inhomogeneous field. To first order in the multi-polar expansion of the field (Equation (1)), the dipolar potential is $V(x,t) = F(x,t)x$, and therefore the quasiparticles experience a linear drift of the momentum:

$$\dot{\kappa}(x,t) = \nabla_x V(x,t) = F_0 \cos(\omega t)\left(1 - 2\alpha k_0 x\right) \quad (2)$$

Because of the position-dependent term, the above equation must be solved simultaneously with the equation of motion $\dot{x} = \nabla_\kappa \varepsilon_g[\kappa(x,t)]$, where $\varepsilon_g(\kappa) = \varepsilon_c(\kappa) - \varepsilon_v(\kappa)$ is the momentum-dependent bandgap of Si. The resulting momentum and position are shown in **Figure 3**a,b, respectively.

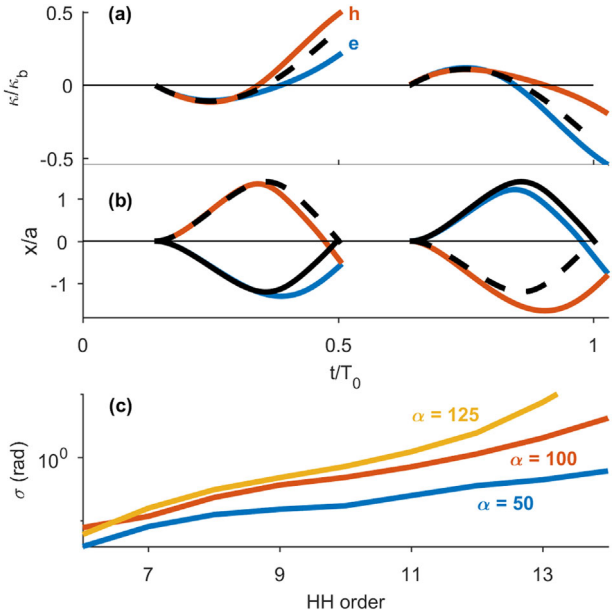

Figure 3. Electron and hole trajectories in the inhomogeneous hotspot. Electrons (blue lines) and holes (red lines) in an inhomogeneous field with $\alpha = 100$ are accelerated to high momenta in the Brillouin zone (panel a, $\kappa_b = \pi/a$, where a = 5.4 Å is the lattice constant of Si, T_0 is the laser period) and to large separations in real space (panel b), but their motion is not mirror-symmetric at two successive laser half-cycles because of the field gradient. In a homogeneous field (black lines, solid for electrons, dashed for holes), the motion is mirror symmetric. Moreover, the electron and the hole separate in reciprocal space, whereas they move in sync in a homogeneous field. c) The phase asymmetry σ increases with the harmonic order and with the gradient parameter α. The field strength is $F_0 = 0.35$ V Å^{-1}. The trajectories shown in panels (a,b) correspond to those responsible for the emission of HH13.

In the homogeneous field ($\alpha = 0$, black dashed lines), the electron and the hole momentum accelerate in sync across the Bril-

louin zone (Figure 3a). In real space (Figure 3b), the electron and hole separate before they recollide, upon which they emit a high-harmonic photon. Trajectories in the inhomogeneous field are also plotted (red lines for holes, blue lines for electrons), for a field gradient parameter $\alpha = 100$, and for an electron-hole pair born at time $t_b = 0.14T_0$ (T_0 is the laser period). In this first-order approximation of the inhomogeneous field, the position of the electron-hole pair at birth is irrelevant. The inhomogeneous field gives electrons and holes different momenta (panel a) and, as a result, the real-space trajectories (panel b) and the time of recollision are modified. In the second half cycle, it is the electron that travels toward the low-field region, and the hole toward the high-field region. Because electrons and holes have different effective masses, the real-space trajectories are not just mirror symmetric with respect to the previous half-cycle, as seen in Figure 3b. For higher field gradients the drift even prevents recollisions altogether (see Data S3, Supporting Information).

The considerations above apply equally to intra- and inter-band high-harmonic emission. In the following, we adopt a model of inter-band (or recollision-based) emission. For a discussion of the effects of asymmetric trajectories on intraband emission see Supporting Information. Moreover, we restrict our analysis to gradients α <125, where the momentum imparted to the electron by the inhomogeneous field remains small compared to the Bloch wavevector $k_b = \pi/a$, where $a = 0.54$ nm is the lattice constant of Si. In addition, higher-order (beyond linear) corrections to the field gradient (Equation (1)) contribute 2% or less at these modest gradients and are thus disregarded. Figure 3a shows that the inhomogeneous field imparts an additional momentum $k/k_b \approx 0.13$ to the trajectories of the 13th harmonic, and this contribution decreases further for the lower harmonics measured in this work. In this regime, the semiclassical equations of motion in homogeneous fields can be utilized. In other words, we only consider vertical transitions. Even though the electron and hole lose momentum overlap, which would prevent the electron-hole pair from recombining through a vertical transition, we assume that some portion of the momentum wavepackets still overlap, thereby leading to recombination and high-harmonic emission, albeit possibly with lower efficiency. Non-vertical contributions can be dominant at higher field gradients, for higher harmonics, and for electron-hole pairs born with non-zero momentum. In this regime, a fully quantum treatment may be required. Reduced overlap between electron and hole wavepackets is a general effect of high-harmonic emission in inhomogeneous fields, even on symmetric antennas.

Given the dissimilarity of the electron-hole pair trajectories at successive laser half cycles, the intensity of even harmonic orders $2n$ is (see Experimental Section):

$$\left|p\left(2n\right)\right|^2 \propto \sin^2\left[\sigma\left(2n\right)\right] \tag{3}$$

where $2\sigma = S_{1/2} - S_1$ is the difference in the semiclassical action acquired by the electron-hole pair wavepacket between two successive half cycles (see Supporting Information). Thus, σ is nearly a direct measurement of the asymmetry of the trajectories. It is plotted in Figure 3c for various field gradients. Intuitively, higher gradients result in stronger even harmonics.

Somewhat counter-intuitively, however, increasing the infrared intensity decreases the degree of asymmetry, and therefore the strength of the even harmonics relative to the neighboring seventh harmonic (**Figure 4**a). The same monotonic trend is predicted for σ, and therefore for the predicted high-harmonic power ratio (Figure 4b). The decreasing asymmetry with increasing field strength arises because the maximum emitted harmonic order (the *cut-off*) increases, which associates a fixed harmonic with increasingly brief electron-hole trajectories. In turn, this leads to the accumulation of smaller semiclassical action and sigma, thus, a smaller asymmetry between successive half cycles (Figure 4c). The observed decrease also suggests that spillover and ionization of the metal antenna,[34] which creates a preferred polarity of the driving field (and thus asymmetry), is negligible in our experimental conditions, since such polarity is expected to increase with field strength. Microscopic particle-in-cell simulations[34] indicate that spillover and ionization effects only arise at higher intensities (see Data S4, Supporting Information).

3. Conclusion

To conclude, we showed that the strong field gradients in plasmonic hotspots perturb the extended electron and hole trajectories and thereby modify the emission of high-order harmonics. Our demonstration bridges high-harmonic and photoelectron experiments, closing the loop on strong-field interactions in nanoscale hotspots. The modified spectrum bears information about the local gradient of the localized field, in both the amplitude – as demonstrated here – and possibly in the phase of the high harmonics. Moreover, our results suggest that shaping the plasmonic hotspots can be a viable method to control the accelerated electron and hole wavepackets directly in the spatial domain on a few-nanometer length scale. In the future, this capability may facilitate tailoring the high-field response of materials such as the efficiency of high-harmonic emission, the spectral distribution, and more, with unprecedented precision.

4. Experimental Section

Simulation of Steady-State Antenna Resonance: An in-house, multiprocessor 3D-FDTD program[35,36] was used to calculate the electromagnetic response of the array of Au triangular nanoantennas on a Si substrate when irradiated by a plane wave. These simulations were high resolution (step-size of 1 nm) to accurately resolve the near fields (see Figure 1b,c). A single unit cell (430 nm x 412 nm) of the metasurface was simulated with periodic boundary conditions. In the propagation direction, there were three layers; a plane-wave source (with a raised cosine envelope[35]) was introduced in the sapphire substrate, and propagated through the Si film, on which there was the plasmonic triangle. The dispersive optical response of Au was modelled with the Drude + 2 Critical Points model.[37] All other materials were treated as dispersionless dielectrics. All simulations were run on the Graham cluster operated by Compute Canada.[38]

Experimental Setup: The experimental setup is sketched in Data S5 (Supporting Information). An amplified Ti:Sapphire laser system (Coherent Legend) delivering 1.3 mJ, 50 fs pulses at 1 kHz repetition rate pumps an optical parametric amplifier (LightConversion TOPAS). The idler beam centered at 2040 nm wavelength, and with a pulse duration of 80 fs, was spatially filtered by focusing it through a diamond die (pinhole). Spurious visible and near-infrared light was filtered with a Si plate, 250 µm thick, rotated to Brewster's angle. A combination of a half-wave plate and wire grid polarizer was utilized to attenuate the power and to set the polarization parallel to the antennas' major axis. A spherical Ag mirror, with

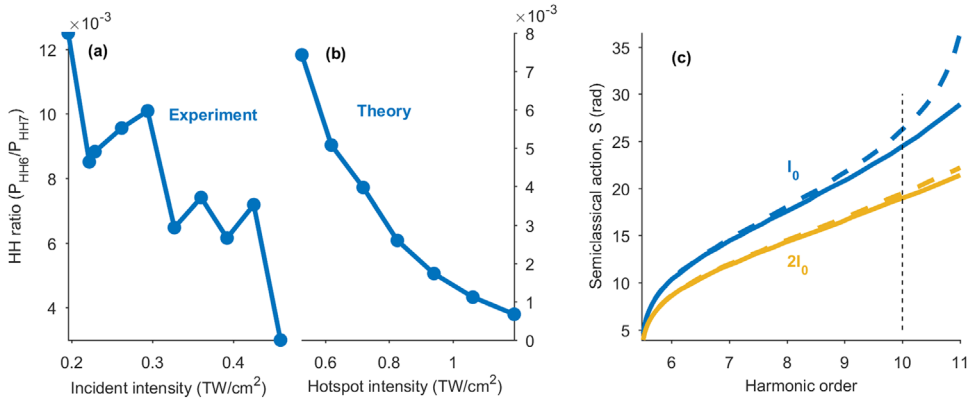

Figure 4. Scaling of asymmetry with laser intensity. The measured degree of asymmetry between HH6 and HH7 decreases with increasing laser intensity (panel a), in agreement with the model (panel b). This is a result of decreasing semiclassical action between successive laser half cycles as the field strength increases (panel c). In (c), blue and yellow lines represent two field strengths of I_0 and $2I_0$, where $I_0 = 0.6$ TW cm^{-2}; solid and dashed lines represent short trajectories in two successive laser half-cycles. The black dashed line marks the tenth harmonic. For all panels, $\alpha = 100$.

100 mm focal length, focused the beam on the sample, which comprised Au nanoantennas on a Si wafer. The generated harmonics were collected in reflection geometry and focused on the slit of a UV–vis spectrometer (Princeton Instruments IsoPlane 320, equipped with PI-MAX4 ICCD camera).

Sample Preparation: Figure 1a and Data S2a (Supporting Information) show scanning electron images of triangular and rectangular nanoantenna arrays fabricated by electron-beam lithography followed by metal evaporation and lift-off, on the surface of a 500 nm thick single-crystal silicon film. Several arrays (60×60 μm^2 area) with slightly different nano-antenna dimensions were fabricated to ensure resonance at the design wavelength. The fabrication details are the same as reported in Ref [22], which is copied below for convenience.

Diced chips were ultrasonically cleaned using acetone and IPA, and then blow-dried using nitrogen for 5 min each. A 2% weight PMMA in anisole solution, with a molecular weight of 450k, was spin-coated at 5000 rpm for 60 s with an acceleration of 1000 rps, and then baked at 180 °C for 30 min, which resulted in a 50 nm thick bottom resist layer. Similarly, a 2% weight PMMA in anisole solution, with a molecular weight of 950k, was used as a second resist layer which was spin-coated at 7000 rpm for 60 s, with an acceleration of 300 rps. The second layer resulted in a 25 nm thick top resist layer. A dose of 360 μCcm^{-2} was used to pattern the nano-antennas by electron beam. The samples were developed in MIBK/IPA (1:3) at 20 °C for 60 s. A 0.5 nm thick titanium adhesion layer was deposited directly on the substrate followed by the evaporation of 20 nm of gold, both using electron-beam evaporation. As a final fabrication step, the metal lift-off took place in an acetone bath at room temperature, which was sonicated at 30 kHz for 30 s, and then blow-dried using nitrogen.

Supporting Information

Supporting Information is available from the Wiley Online Library or from the author.

Acknowledgements

It is the authors pleasant duty to acknowledge David Crane, Ryan Kroeker, and Andrei Naumov for providing continuing technical support. G.V., L.R., and S.A.J. acknowledge financial support from the Joint Center for Extreme Photonics. K.M.A. acknowledges the support of the Advanced Nanofab Facility of the Stewart Blusson Quantum Matter Institute and SiEPIC Fab for the fabrication of the plasmonic array sample. T.F. acknowledges support by the Deutsche Forschungsgemeinschaft (DFG, German Research Foundation) via the SFB 1477 "light–matter interactions at interfaces" (project number 441234705) and via the Heisenberg program (project number 436382461).

Conflict of Interest

The authors declare no conflict of interest.

Data Availability Statement

The data that support the findings of this study are available from the corresponding author upon reasonable request.

Keywords

high-harmonic generation, inhomogeneous near-fields, plasmonic metasurfaces

Received: May 17, 2023
Revised: August 22, 2023
Published online: October 20, 2023

[1] B. Wolter, M. G. Pullen, A. T. Le, M. Baudisch, K. Doblhoff-Dier, A. Senftleben, M. Hemmer, C. D. Schröter, J. Ullrich, T. Pfeifer, R. Moshammer, S. Gräfe, O. Vendrell, C. D. Lin, J. Biegert, *Science* **2016**, *354*, 308.
[2] M. Kübel, Z. Dube, A. Y. Naumov, D. M. Villeneuve, P. B. Corkum, A. Staudte, *Nat. Commun.* **2019**, *10*, 1042.
[3] G. Porat, G. Alon, S. Rozen, O. Pedatzur, M. Krüger, D. Azoury, A. Natan, G. Orenstein, B. D. Bruner, M. J. J. Vrakking, N. Dudovich, *Nat. Commun.* **2018**, *9*, 2805.
[4] M. Ossiander, F. Siegrist, V. Shirvanyan, R. Pazourek, A. Sommer, T. Latka, A. Guggenmos, S. Nagele, J. Feist, J. Burgdörfer, R. Kienberger, M. Schultze, J. Feist, J. Burgdörfer, *Nat. Phys.* **2017**, *13*, 280.
[5] P. M. Kraus, B. Mignolet, D. Baykusheva, A. Rupenyan, L. Horný, E. F. Penka, G. Grassi, O. I. Tolstikhin, J. Schneider, F. Jensen, L. B. Madsen, A. D. Bandrauk, F. Remacle, H. J. Wörner, *Science* **2015**, *350*, 790.

[6] A. D. Shiner, B. E. Schmidt, C. Trallero-Herrero, H. J. Wörner, S. Patchkovskii, P. B. Corkum, J. C. Kieffer, F. Légaré, D. M. Villeneuve, *Nat. Phys.* **2011**, *7*, 464.
[7] A. L. Cavalieri, N. Müller, T. Uphues, V. S. Yakovlev, A. Baltuska, B. Horvath, B. Schmidt, L. Blümel, R. Holzwarth, S. Hendel, M. Drescher, U. Kleineberg, P. M. Echenique, R. Kienberger, F. Krausz, U. Heinzmann, *Nature* **2007**, *449*, 1029.
[8] S. Ghimire, A. D. Dichiara, E. Sistrunk, P. Agostini, L. F. Dimauro, D. A. Reis, *Nat. Phys.* **2011**, *7*, 138.
[9] T. T. Luu, M. Garg, S. Y. Kruchinin, A. Moulet, M. T. Hassan, E. Goulielmakis, *Nature* **2015**, *521*, 498.
[10] G. Vampa, T. J. Hammond, N. Thiré, B. E. Schmidt, F. Légaré, C. R. Mcdonald, T. Brabec, P. B. Corkum, *Nature* **2015**, *522*, 462.
[11] O. Schubert, M. Hohenleutner, F. Langer, B. Urbanek, C. Lange, U. Huttner, D. Golde, T. Meier, M. Kira, S. W. Koch, R. Huber, *Nat. Photonics* **2014**, *8*, 119.
[12] Y. S. You, D. A. Reis, S. Ghimire, *Nat. Phys.* **2017**, *13*, 345.
[13] M. Krüger, M. Schenk, P. Hommelhoff, *Nature* **2011**, *475*, 78.
[14] G. Herink, D. R. Solli, M. Gulde, C. Ropers, *Nature* **2012**, *483*, 190.
[15] F. Süßmann, L. Seiffert, S. Zherebtsov, V. Mondes, J. Stierle, M. Arbeiter, J. Plenge, P. Rupp, C. Peltz, A. Kessel, S. A. Trushin, B. Ahn, D. Kim, C. Graf, E. Rühl, M. F. Kling, T. Fennel, *Nat. Commun.* **2015**, *6*, 7944.
[16] L. Seiffert, Q. Liu, S. Zherebtsov, A. Trabattoni, P. Rupp, M. Castrovilli, M. Galli, F. Süßmann, K. Wintersperger, J. Stierle, *Nat. Phys.* **2017**, *13*, 766
[17] J. Schötz, L. Seiffert, A. Maliakkal, J. Blöchl, D. Zimin, P. Rosenberger, B. Bergues, P. Hommelhoff, F. Krausz, T. Fennel, M. F. Kling, *Nanophotonics* **2021**, *10*, 3769.
[18] J. Passig, S. Zherebtsov, R. Irsig, M. Arbeiter, C. Peltz, S. Göde, S. Skruszewicz, K. H. Meiwes-Broer, J. Tiggesbäumker, M. F. Kling, T. Fennel, *Nat. Commun.* **2017**, *8*, 1181.
[19] L. Seiffert, T. Paschen, P. Hommelhoff, T. Fennel, *J. Phys. B: At. Mol. Opt. Phys.* **2018**, *51*, 134001.
[20] G. Vampa, B. G. Ghamsari, S. Siadat Mousavi, T. J. Hammond, A. Olivieri, E. Lisicka-Skrek, A. Y. Naumov, D. M. Villeneuve, A. Staudte, P. Berini, P. B. Corkum, *Nat. Phys.* **2017**, *13*, 659.
[21] S. Han, H. Kim, Y. W. Kim, Y. J. Kim, S. Kim, I. Y. Park, S. W. Kim, *Nat. Commun.* **2016**, *7*, 13105.
[22] S. A. Jalil, K. M. Awan, I. A. Ali, S. Rashid, J. Baxter, A. Korobenko, G. Ernotte, A. Naumov, D. M. Villeneuve, A. Staudte, P. Berini, L. Ramunno, G. Vampa, *Optica* **2022**, *9*, 987.
[23] M. Sivis, M. Taucer, G. Vampa, K. Johnston, A. Staudte, A. Y. Naumov, D. M. Villeneuve, C. Ropers, P. B. Corkum, *Science* **2017**, *357*, 303.
[24] H. Liu, C. Guo, G. Vampa, J. L. Zhang, T. Sarmiento, M. Xiao, P. H. Bucksbaum, J. Vuckovic, S. Fan, D. A. Reis, *Nat. Phys.* **2018**, *14*, 1006.
[25] H. Liu, G. Vampa, J. L. Zhang, Y. Shi, S. Buddhiraju, S. Fan, J. Vuckovic, P. H. Bucksbaum, D. A. Reis, *Commun. Phys.* **2020**, *3*, 192.
[26] M. R. Shcherbakov, H. Zhang, M. Tripepi, G. Sartorello, N. Talisa, A. Alshafey, Z. Fan, J. Twardowski, L. A. Krivitsky, A. I. Kuznetsov, E. Chowdhury, G. Shvets, *Nat. Commun.* **2021**, *12*, 4185.
[27] G. Zograf, K. Koshelev, A. Zalogina, V. Korolev, R. Hollinger, D. Y. Choi, M. Zuerch, C. Spielmann, B. Luther-Davies, D. Kartashov, S. V. Makarov, S. S. Kruk, Y. Kivshar, *ACS Photonics* **2022**, *9*, 567.
[28] P. B. Corkum, *Phys. Rev. Lett.* **1993**, *71*, 1994.
[29] G. Vampa, T. Brabec, *J. Phys. B: At., Mol. Opt. Phys.* **2017**, *50*, 083001.
[30] A. Gorlach, O. Neufeld, N. Rivera, O. Cohen, I. Kaminer, *Nat. Commun.* **2020**, *11*, 4598.
[31] M. F. Ciappina, J. Biegert, R. Quidant, M. Lewenstein, *Phys. Rev. A* **2012**, *85*, 033828.
[32] A. Husakou, S. J. Im, J. Herrmann, *Phys. Rev. A* **2011**, *83*, 043839.
[33] K. O'brien, H. Suchowski, J. Rho, A. Salandrino, B. Kante, X. Yin, X. Zhang, *Nat. Mater.* **2015**, *14*, 379.
[34] C. Varin, C. Peltz, T. Brabec, T. Fennel, *Phys. Rev. Lett.* **2012**, *108*, 175007.
[35] A. C. Lesina, A. Vaccari, P. Berini, L. Ramunno, *Opt. Express* **2015**, *23*, 10481.
[36] J. Baxter, A. C. Lesina, L. Ramunno, *IEEE Trans. Antennas Propag.* **2020**, *69*, 3982.
[37] K. P. Prokopidis, D. C. Zografopoulos, *J. Lightwave Technol.* **2013**, *31*, 2467.
[38] G. docs.alliancecan.ca/wiki/Graham.